ACS Photonics

Open Access

pubs.acs.org/journal/apchd5

Article

Tunable Nanoislands Decorated Tapered Optical Fibers Reveal Concurrent Contributions in Through-Fiber SERS Detection

Di Zheng,* Muhammad Fayyaz Kashif, Linda Piscopo, Liam Collard, Cristian Ciracì, Massimo De Vittorio,*,⊥ and Ferruccio Pisanello*,⊥

Cite This: ACS Photonics 2024, 11, 3774−3783

Read Online

ACCESS | Metrics & More | Article Recommendations | Supporting Information

ABSTRACT: Creating plasmonic nanoparticles on a tapered optical fiber (TF) tip enables a remote surface-enhanced Raman scattering (SERS) sensing probe, ideal for challenging sampling scenarios like biological tissues, site-specific cells, on-site environmental monitoring, and deep brain structures. However, nanoparticle patterns fabricated from current bottom-up methods are mostly random, making geometry control difficult. Uneven statistical distribution, clustering, and multilayer deposition introduce uncertainty in correlating device performance with morphology. Ultimately, this limits the design of the best-performance remote SERS sensing probe. Here we employ a tunable solid-state dewetting method to create densely packed monolayer Au nanoislands with varied geometric parameters in direct contact with the silica TF surface. These patterns exhibit analyzable nanoparticle sizes, densities, and uniform distribution across the entire taper surface, enabling a systematic investigation of particle size, density, and analyte effects on the SERS performance of the through-fiber detection system. The study is focused on the SERS response of a widely employed benchmark molecule, rhodamine 6G (R6G), and serotonin, a highly relevant neurotransmitter for the neuroscience field. The numerical simulations and limit of detection (LOD) experiments on R6G show that the increase of the total near-field enhancement volume promotes the SERS sensitivity of the probe. However, we observed a different behavior for serotonin linked to its interaction with the nanoparticle's surface. The obtained LOD is as low as 10^{-7} M, a value not achieved so far in a through-fiber detection scheme. Therefore, our work offers a strategy to design nanoparticle-based remote SERS sensing probes and provides new clues to discover and understand intricate plasmonic-driven chemical reactions.

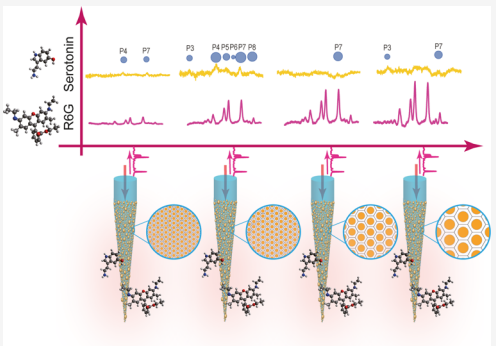

KEYWORDS: *solid-state dewetting, tunable, nanoislands, SERS, tapered optical fiber, neurotransmitter*

INTRODUCTION

Molecular sensing based on surface-enhanced Raman scattering (SERS) has shown promise as a powerful analytical tool for biomedical diagnostics, identification of chemical compounds, food safety, and environmental monitoring.[1−4] A frontier for SERS is represented by the ability to perform label-free and chemical-specific sensing in applications where sampling is difficult, including (i) probing biological tissue,[5,6] (ii) site-specific study for living cells,[7,8] and (iii) on-site environmental monitoring, such as detection for hazardous heavy metal and toxic gas.[9−11] Integrating a SERS substrate on a fiber optic probe can create a compact and multifunctional sensor that can be used as a point-of-care SERS amplifier or remote sensing probe where the excitation laser and the resulting Raman signal are guided and collected by the same waveguide (the through-fiber detection scheme). Additionally, the ability to implement SERS in small-diameter optical fibers[12,13] has the potential to extend SERS applications to environments where sample perturbations need to be minimized, such as brain structures. In the context of studying neurochemical dynamics, vibrational spectroscopy enhanced by plasmonic nanostructures is of particular interest by its ability to detect and identify neurotransmitters even at attomolar concentrations,[14] with the release of these molecules linked to both physiological and pathological states, including Alzheimer's disease, depression, schizophrenia, and Parkinson's disease.[15−18]

SERS-active fiber optic probes have been mainly fabricated by covering the termination of an optical fiber with metallic nanoparticles.[19−31] Of specific significance is the case of tapered optical fibers (TFs), the plasmonic structures on the TF surface can engage with both radiative and guided modes over a customizable segment ranging from a few hundred micrometers to several millimeters.[32] Some guided modes can radiate out by thinning the fiber waveguide, while the remaining guided modes in the waveguide create evanescent

Received: May 25, 2024
Revised: August 9, 2024
Accepted: August 9, 2024
Published: August 28, 2024

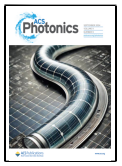

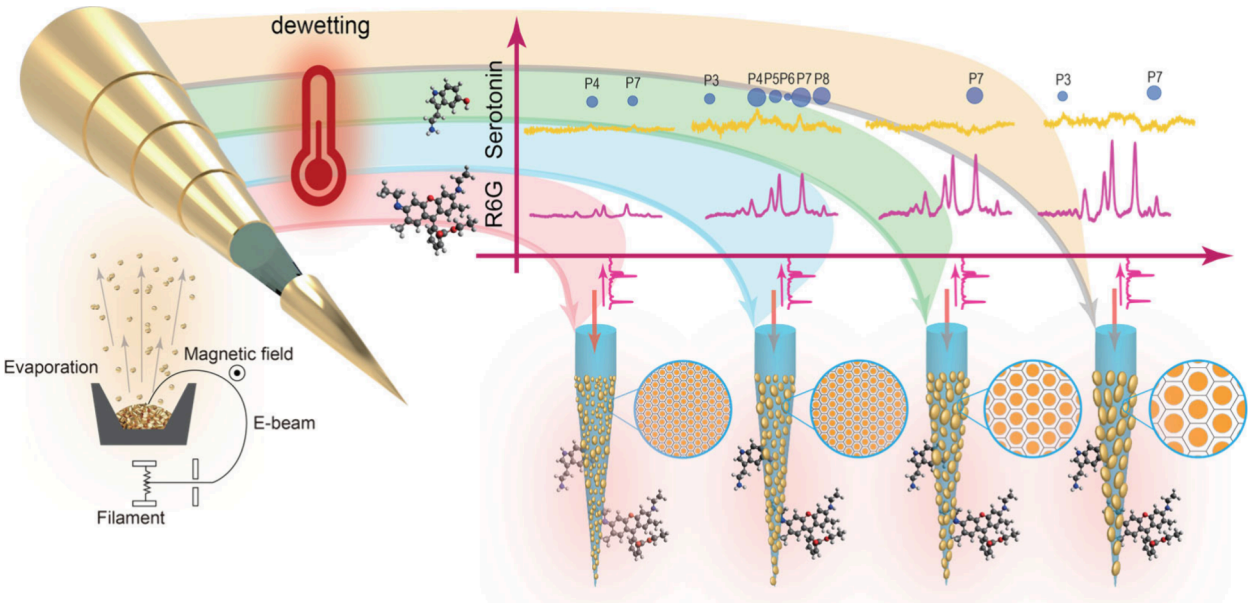

Figure 1. Schematic illustration of the fabrication and characterization for tunable NIs-TF probes. The thicker the initial gold film deposition, the dewetting output generates bigger NIs diameters and gaps. The through-fiber SERS sensing for R6G and serotonin was analyzed from four different types of TFs with tunable NIs patterns; the enlarged window beside each tapered fiber illustrates the statistical particle size and density on the same scale.

fields at the surface.[12,33,34] Both types of fields can interact with plasmonic structures covering the entire tapered surface, expanding the sensing areas that can interact with the surrounding environment. Additionally, the wide and uniform interaction surface of the NIs-covered taper can be used for depth-selective SERS measurement if taking advantage of its mode-division demultiplexing.[35] Moreover, the tapered shape reduces invasiveness when interfacing with deep brain structures, making it more suitable and effective for neurological studies. Fabricating plasmonic structures on the TFs requires the structuring of a curved surface with a nonconstant curvature radius. Only bottom-up approaches have been demonstrated to successfully enable SERS sensing capabilities on a TF probe, including electrostatic self-assembly,[10,27,36−43] direct nucleation reaction,[44−47] dip coating, and laser-assisted evaporation.[23,48−51] However, plasmonic nanoparticle distributions on the surface fabricated by these approaches are largely random. The morphologies show an uneven statistical distribution across the large surface, cluster formation, and multilayer deposition, inevitably introducing uncertainty and ambiguity on the correlation between the device performance and the morphological status, limiting the understanding and design of the best-performance remote sensing tapered SERS probe.

Here, we aim at uncovering the correlation between particle size and density versus the probe's SERS performance, to provide design principles for particle-decorated TF remote sensing probes. A tunable solid-state dewetting technology was employed to fabricate nanoislands (NIs) with varied geometric parameters. The monolayer densely packed NIs are surfactant-free and in direct contact with the silica surface of TFs. The formed patterns have analyzable nanoparticle sizes, densities, and statistically uniform distributions through the entire extent of the taper's surface. This allows us to systematically study, for the first time, the effect of the particle size, density, and analyte on the overall SERS performance of the through-fiber detection system.

By incrementally increasing the thickness of the deposited gold film, NIs patterns with gradually increased average diameters, heights, and gaps, were obtained. These increased NIs unit cells were numerically modeled to match with the statistically analyzed nonplanar NIs patterns, finding that increasing NIs unit cells corresponds to increasing volume field enhancement (VFE) across the entire tapered fiber surface, thereby resulting in a gradual increase in SERS signals. Experimental evaluations were then performed with 785 nm excitation on four NIs-TFs configurations with gradually increased NIs unit cells, with rapid through-fiber SERS experiments that do not require a prolonged immersion in the analyte's solution. First, the commonly used Raman reporter rhodamine 6G (R6G) was used as the target analyte, due to its stable chemical composition and distinct Raman peaks. Across 4 different patterns of NIs-TFs probes, a stable limit of detection (LOD) of 10^{-6} M was obtained, while the spectral amplification gradients show that the increasing NIs unit cell facilitates SERS detection, aligning with the theoretical predictions on the VFE. Expanding the study to monoamine neurotransmitters, the use of serotonin as a target analyte revealed a different trend. The highest sensitivity (jointly considering the lowest LOD, number of detected peaks, and peak prominence) was obtained with the second smallest NIs unit cells TF probes with a LOD of 10^{-7} M, which is, to the best of our knowledge, the lowest value to date in a through-fiber detection configuration. Unlike the spectral response of R6G, the serotonin spectral response shows sensitivity performance favoring small NIs unit cells. The notable attributes indicate that chemical reactions involving serotonin, driven by plasmonics, are occurring at the interface.

RESULTS

Figure 1 shows schematic steps for fabricating NIs patterns with different geometrical parameters on the nonplanar surface of the fiber taper. TFs were obtained by a heat-and-pull method from commercially available core/cladding step-index

https://doi.org/10.1021/acsphotonics.4c00912
ACS Photonics 2024, 11, 3774−3783

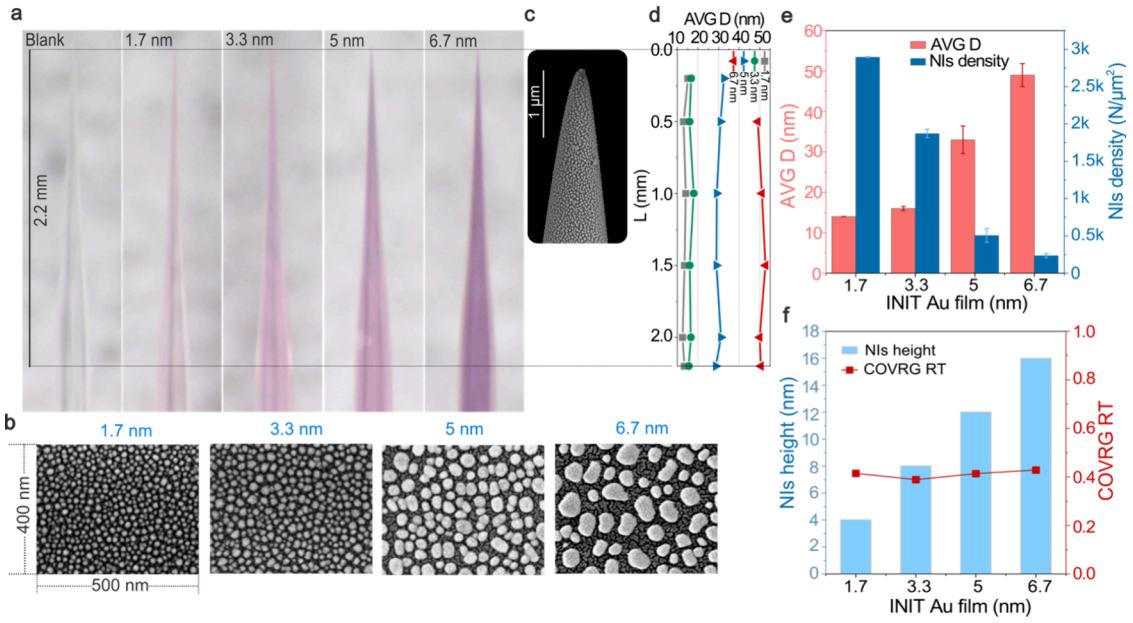

Figure 2. Fabrication output for the tunable NIs-TFs set. (a) Optical images of a representative tunable NIs-TFs set. The blank TF on the left is used as color contrast reference, and the following NIs-TFs from left to right are fabricated with initial Au film coatings of 1.7, 3.3, 5, and 6.7 nm, respectively. (b) SEM images showing the representative morphologies for NIs-TFs with initial Au film coatings of 1.7, 3.3, 5, and 6.7 nm, respectively. (c) SEM images of an enlarged view at the NIs-TF tip (initial Au film of 5 nm). (d) NIs average diameter distributions along the TF for a tunable NIs-TFs set. (e) Statistical analysis showing the average diameter (red bars) and the NIs density (blue bars) with the step-increased initial Au film thickness. (f) Coverage rate (red squares) and NIs height (light-blue bars) for each initial Au film thickness.

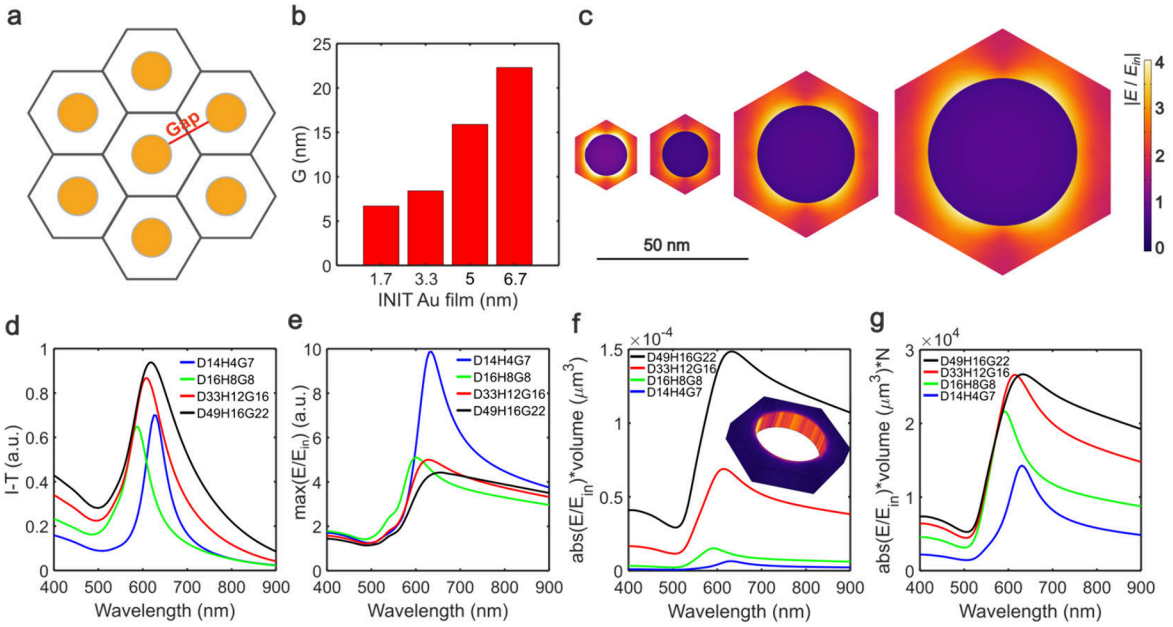

Figure 3. Electromagnetic simulations based on SEM morphologies. (a) Illustration of periodic hexagonal NIs arrays. The red line indicates the gap. (b) Calculated gaps according to hexagonal NIs patterns. (c) Near-field enhancement distribution at 785 nm for four morphologies and the relative sizes of four unit cells corresponding with the real size ratio. (d) Plasmonic resonances, reported as $1 - T$ for four morphologies of NIs patterns, where T is the calculated transmittance. (e) Maximum near-field enhancement along with different wavelengths produced by each morphology as a function of the incident wavelength under normal incidence. (f) Volumetric near-field enhancement, calculated by integrating the near-field enhancement over the hollow hexagonal prism surrounding the NIs, as shown in the inset. (g) Volumetric near-field enhancement multiplied by the number of unit cells that can occupy the whole taper fiber surface.

silica fibers. By incrementally increasing the deposited gold film's thickness, after dewetting, NIs' patterns can be tuned (for details, see section S1).

For the experimental demonstration, we fabricated four sets of NIs-TFs with initial film thicknesses of Thk_i = 1.7, 3.3, 5, and 6.7 nm. Under an optical microscope, the surface of the four sets of NIs-TFs at growing thickness shows a gradually increasing pink color (Figure 2a), generated by an increase in NIs' size as identified by scanning electron microscope (SEM) (Figure 2b). To extract the geometric parameters of the NIs

https://doi.org/10.1021/acsphotonics.4c00912
ACS Photonics 2024, 11, 3774−3783

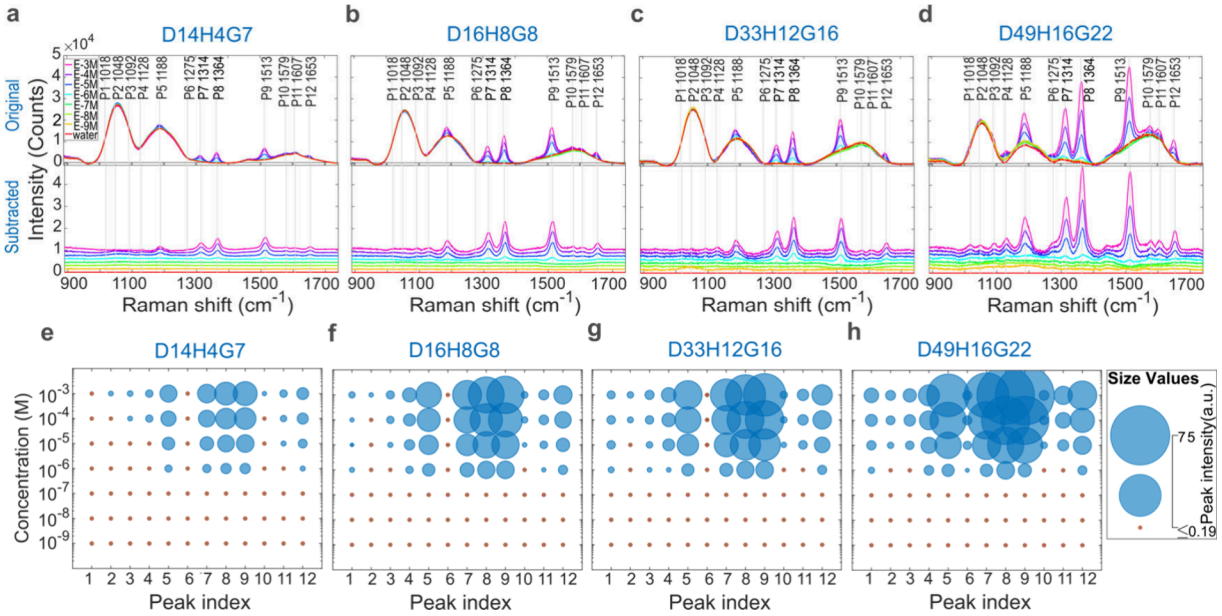

Figure 4. Limit of detection experiment for aqueous solution of R6G with tunable NIs-TFs set. (a–d) SERS spectra sets for tunable NIs-TFs with four NIs patterns (D14H4G7, D16H8G8, D33H12G16, and D49H16G22). The spectra in the top panels are the original spectra, and the spectra in the bottom panels are the silica-background-subtracted spectra (the silica background was taken as the spectrum measured in water). Before the subtraction, the original spectra were normalized to the silica peak at 1055 cm^{-1}. The subtracted spectra have been vertically offset for clarity. The vertical lines mark the 12 R6G peak positions. (e–h) Bubble chart of 12 R6G peaks. The sizes of the blue bubbles correspond to integrated peak areas, and the small orange bubbles mark peak absences.

patterns quantitatively, SEM image batches were taken along the entire extent of the fiber taper (a representative high magnification image at the very tip of TF is shown in Figure 2c). Image recognition methods (described in Methods) were used to compute the coverage rate, particle number and particle density for each image. For the different Au film thicknesses, 2 TFs were included in the analysis. For each fiber, the number of sampled images with different magnifications along the taper was no less than 10. The measured average diameters at different taper positions are reported in Figure 2d, showing that the different NIs patterns distribute uniformly from the very tip to the taper end. The final geometric parameters of NIs' patterns were then extracted by averaging between two fibers, and each statistic is an averaging of all the data points at different positions along the whole taper. Figure 2e shows the average diameters and NIs' densities calculated, the diameters are $D_1 = 14 \pm 2$, $D_2 = 16 \pm 2$, $D_3 = 33 \pm 3$, and $D_4 = 49 \pm 3$ nm, and the NIs densities are $\rho_1 = 2895 \pm 7$, $\rho_2 = 1872 \pm 57$, $\rho_3 = 507 \pm 93$, and $\rho_4 = 236 \pm 27$ NIs/μm^2, for the ith Thk_i (i = 1, 2, 3, 4). Figure 2f displays the coverage rates (C) for the four different patterns, found to be about 40%, independent of initial film thickness, and the corresponding average heights (H_i) of the NIs are H_i = 4, 8, 12, and 16 nm (computed with $H_i = Thk_i/C_i$).

To understand the electromagnetic performances of the different NIs patterns, we implemented a model with Au nanodisks arranged in a hexagonal periodic manner (Figure 3a). One nanodisk of diameter D occupies the center of a hexagonal unit cell. The diameters of the nanodisks are the average diameters for each pattern in Figure 2e. The heights of the nanodisks are taken from Figure 2f as $H_i = Thk_i/C_i$. The ratio between nanodisk's occupied surface and the overall unit cell area in 2D plane defines the coverage rates, which equal the coverage rates obtained from SEM image analysis (Figure 2f). Given the experimental average values for D and C as a function of Thk, the resulting effective gaps (G) in a hexagonal periodic arrangement can be computed to be 7, 8, 16, and 22 nm (Figure 3b; details in Methods). These geometric parameters define the NIs patterns and, hereinafter, we mark the patterns fabricated by initial film coating of Thk_i = 1.7, 3.3, 5, and 6.7 nm as D14H4G7, D16H8G8, D33H12G16, and D49H16G22 respectively.

The electromagnetic behavior of the structures was simulated by a finite element method (commercial implementation by COMSOL Multiphysics) with an unpolarized plane wave excitation source. Representative field enhancement distributions at 785 nm in one unit cell are displayed in Figure 3c. The plasmonic resonances are shown as the complement of transmittance in Figure 3d: as each pattern has different geometric parameters, the plasmonic resonances of the systems are slightly different in terms of position, intensity, and spectral width. The maximum field enhancements as a function of wavelength are reported in Figure 3e, showing that at above 595 nm the smallest NIs D14H4G7 give the strongest field enhancement, the cross-section of the field enhancement is reported in Figure S2. Although the field enhancement localized by the NIs is distributed on all edges, the interaction between the molecules and the particles requires spatial overlap. This excludes the region below the NIs since there is the silica fiber substrate. Therefore, the regions where the excitation light interacts with the target molecules include the spaces close to both the top and side surfaces of the Au nanoparticles. Assuming that analytes are distributed uniformly in the surrounding environment, the absolute amount of the SERS signal for each unit cell correlates with the field enhancement integral in the space with nonzero field distribution (i.e., everywhere in the unit cell apart from the nanodisk). To better quantify the effect of electric field enhancement on the SERS performance, we calculated the VFE by integrating the local filed enhancement E/E_{in} over the

https://doi.org/10.1021/acsphotonics.4c00912
ACS Photonics 2024, 11, 3774–3783

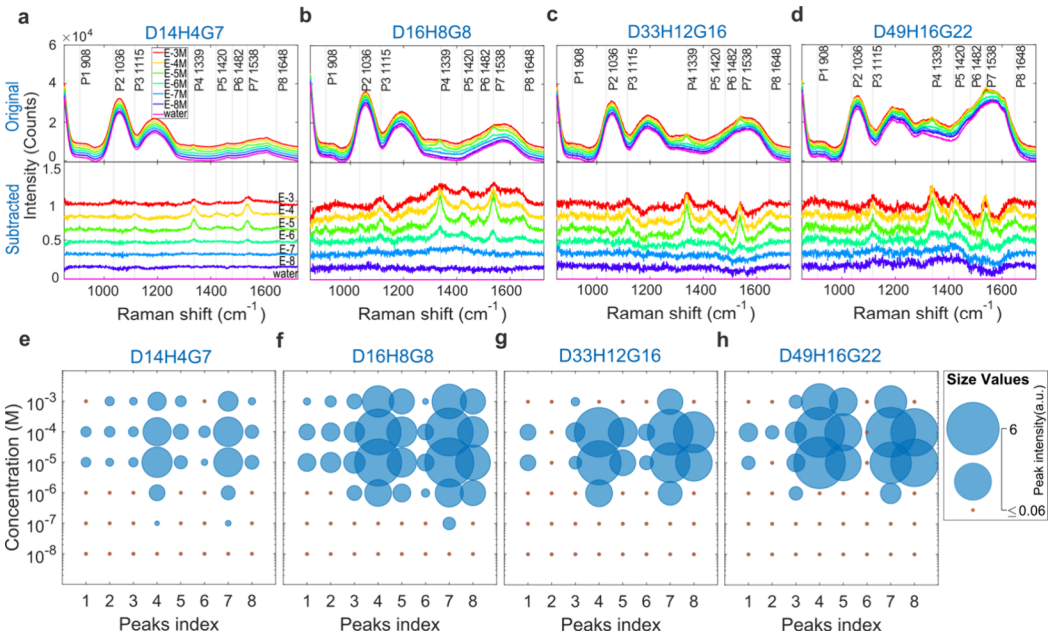

Figure 5. Limit of detection experiment for aqueous solutions of serotonin with tunable NIs-TFs set. (a–d) SERS spectra sets for tunable NIs-TFs with four NIs patterns (D14H4G7, D16H8G8, D33H12G16, and D49H16G22). The spectra in the top panels are the original spectra, and the spectra in the bottom panels are the silica-background-subtracted spectra (the silica background was taken as the spectrum measured in water). Before the subtraction, the original spectra were normalized to the silica peak at 1055 cm^{-1}. The spectra sets have been vertically offset for clarity. The vertical lines mark the 8 serotonin peak positions. (e–h) Bubble chart of 8 serotonin peaks. The sizes of the blue bubbles correspond to integrated peak areas, and the small orange bubbles mark peak absences.

volume of one unit cell, taken as an extruded hexagon around the nanodisk rising 10% over the nanodisks' height (inset in Figure 3f, cross-section in Figure S2, VFE normalized to unit volume in Figure S3). The calculated VFE shows that at all analyzed wavelengths, D49H16G22 has the strongest VFE, followed by D33H12G16, D16H8G8, and D14H4G7 (Figure 3f). Assuming that such patterns cover the entire fiber surface, we have estimated the number of unit cells N that covers the conical taper surface (see Methods). For a fixed surface area, the smaller NIs system will contain more unit cells than the bigger particles. Figure 3g reports the unit cell VFE multiplied by N for each pattern, showing that for most of the wavelength regions on which the calculations were performed the bigger particle patterns experience the higher absolute field enhancement (except for 570 to 620 nm). These results suggest that if the electromagnetic effect is the main contribution to the overall SERS signal, the larger particle pattern will generate the highest SERS scattered signal.

To verify the correlation of the NIs-TFs's performances with the 4 different NIs patterns on the TF surface, we conducted through-fiber SERS measurements in solution. We first used R6G as a chemically stable analyte to test the LOD of the probes. Different concentrations (from 10^{-9} to 10^{-3} M) of R6G aqueous solutions were prepared, and then through-TF SERS measurements were conducted with a custom-built Raman microscope (details in Methods). For each NIs-TF, the measurements started from the lowest concentration solution and increased toward the highest concentration in steps, using a single fiber for each concentration ramp. Each spectrum was taken immediately after the fiber tip was immersed entirely into the aqueous solution, and the fiber tip was kept in the solution only during the exposure time. Four different patterns (D14H4G7, D16H8G8, D33H12G16 and D49H16G22) of the NIs-TFs set were tested, with n = 2 fibers for each pattern. The measured spectra at different concentrations are reported in Figure 4a–d, in the original spectra, they are composed of a contribution from the analyte and a Raman background generated by the probe itself. This latter is not the same for the four NIs patterns (Figure S7). To improve the visibility and contrast of the analyte's signal, a reference spectrum method was employed to subtract the silica background. This process began by acquiring the fiber Raman background from clean samples in water without any analytes present. Then, the analyte's signal was obtained by subtracting the fiber background from the original SERS spectrum, as shown in the bottom panels of Figure 4a–d. For all types of NI-TFs, the R6G Raman signature can be identified from 10^{-6} M, and the peak intensities increase as the NIs grow. Among all the subtracted spectra, 12 R6G Raman peaks were identified (1018, 1048, 1092, 1128, 1188, 1275, 1314, 1364, 1513, 1579, 1607, 1653 cm^{-1}). In Figure 4e–h, a more detailed data analysis is presented with the bubble charts, allowing a better comparison between the different samples. The raw spectra were first normalized to the silica peak at 1055 cm^{-1}, then the silica background measured in water was subtracted from the normalized spectra. Working on the subtracted normalized spectra set, the 12 peaks were analyzed individually. A local linear baseline was removed from each peak, then we integrated the area of each peak. The summation of the corresponding peak intensities of the two data sets was used as a marker for the bubble sizes in the bubble chart (see Figure S5 for more details). For all 4 types of patterns, R6G signature peaks appear at the concentration of 10^{-6} M. Most of the peaks increase in intensity concurrently as concentration increases, and the patterns comprised of larger NI's, result in a more intense R6G SERS signal with a direct correlation to the total VFE increase.

https://doi.org/10.1021/acsphotonics.4c00912
ACS Photonics 2024, 11, 3774–3783

To broaden our findings beyond R6G, we employed NI-TFs to detect serotonin. This monoamine neurotransmitter, smaller than R6G and showing a stronger affinity for gold, influences numerous neurological functions and is implicated in conditions like depression and anxiety.[52,53] Thus, tunable NIs-TFs sets with $n = 2$ fibers per pattern were measured. The representative spectra data sets and the corresponding subtracted spectra sets are shown in Figure 5a−d. The same data analysis approach as R6G was adopted (details in Figure S5). There are 8 peaks identifiable across all the spectra data sets, at 908, 1036, 1115, 1339, 1420, 1482, 1538, and 1648 cm^{-1}. The detailed analysis results are shown in the bubble chart in Figure 5e−h. Interestingly, for serotonin, more peaks and lower LOD (10^{-7} M) are obtained with smaller NIs patterns (D14H4G7 and D16H8G8). Additionally, from all the data sets there is an obvious degradation of the detection capability (or even vanishing) at high concentrations. Further tests on the probe that degraded at high serotonin concentrations show that it is still able to detect R6G molecules but with less peak intensity and one order of decreased detection sensitivity at 10^{-5} M (detailed data presented in Figure S6). Considering the lowest LOD, the peak numbers, and the spectra prominence, D16H4G8 NIs patterns show the best performance.

The spectra of R6G and serotonin show both similarities and differences. Commonly, the 1055 cm^{-1} silica peak is stable, while higher wavenumber silica background increases with NI size (Figure S7), indicating wavelength-selective modulation of reflection/transmission ratios. Differences include: (i) With increasing concentration, R6G peak intensities rise, while serotonin peaks degrade, especially at higher concentrations. (ii) R6G shows more peaks with higher total VFE, while serotonin does so with lower total VFE. (iii) Smaller NIs with narrower gaps (D16H8G8) can achieve a lower LOD for serotonin with minimal peak intensity changes, while R6G peak prominence increases with higher total VFE.

DISCUSSION AND CONCLUSION

In a through-fiber detection setup with plasmonic NIs-TFs, various factors impact SERS signal detection of a target analyte. These include: (1) NIs patterns' near-field enhancement, (2) relative strength between molecular SERS signal and fiber-generated Raman background, (3) analyte interaction with gold NIs, and (4) spatial overlap between analytes and near-field enhancement. Our study shows distinct influences of these factors on R6G and serotonin, a neurologically relevant neurotransmitter.

For R6G, our experiments show that the total VFE of the tunable NIs patterns on the taper surface mainly dominates the spectral response. The higher SERS signals can be obtained along with gradually increased total VFE. The modulation on the background reflection does not affect the intensity of characteristic peaks significantly, since R6G has a large Raman cross-section which can provide high relative strength when mixing with the silica Raman background from the fiber. R6G does not possess functional groups with a strong affinity to gold (therefore it is unlikely that R6G will bond on NIs and generate surface chemical reactions), and the spectral response is stable with well-recognized molecular vibrations.[54,55] Additionally, the molecular size of R6G (~1 nm[56,57]) is well below the narrowest investigated gap (~7 nm). Given the low gold affinity and this factor, we hypothesize a uniform spatial overlap between R6G molecules and near-field enhancement, aligning with assumptions in our simulations.

For serotonin, its small Raman cross-section results in a weak signal (relative to fiber background), which makes the modulation of the background have more impact on the detection of serotonin peaks. Thus, the increasing background observed as a function of the NI's size is more likely to diminish the peaks' prominence at low concentrations. This may explain the lower LOD obtained for samples D14H4G7 and D16H8G8. Smaller serotonin molecules, roughly 60% the size of R6G, with amino functional groups, can bond to gold surfaces more effectively,[58−62] especially in narrow gap regions and near the surface, even at low concentrations. This results in better spatial overlap between molecules and more intense 'hot spots' generated by narrower gaps in smaller NIs patterns like D14H4G7 and D16H8G8. Along with concentration increase, the increased density of serotonin bonded on the gold surface might induce a polymerization reaction[63] forming a Raman inactive dielectric layer dampening the SERS sensitivity at high concentrations ($\geq 10^{-4}$ M). The interplay of all those factors results in the serotonin spectra response shown in Figure 5. The serotonin SERS bands vary in the literature due to factors like excitation wavelength, dissolving environments, and nanometal materials used.[14,64−66] Peak disappearance and shifts have been noted in indole ring modes.[67] Studies often focus on thiol molecules due to their strong bonding with Au surfaces.[68−71] For instance, 4-nitrobenzenethiol (NBT) can dimerize into 4,4′-dimercaptoazobenzene (DMAB) under laser radiation, showing new peaks in the SERS spectrum.[68] Au nanoparticles on microsphere systems have shown similar reactions.[71]

In pursuit of improved sensitivity for SERS probes, another important aspect we should consider is the collection properties of the SERS signal for nanoparticle-decorated fiber probes. Different from the volumetric collection scheme of the blank TF,[35] the collection of nanoparticle-decorated TF mainly happens at the interface. The NIs on the tapered fiber surface are first excited by the fiber photonic-guided and radiative modes, forming the local field enhancement around the NIs' surfaces, which are so-called "hot spots". When molecules are in those hot spots, a Raman dipole can be generated. The NIs then work as antennas to convert that evanescent molecular source field to propagating far-field radiation, and the plasmonic mode dominates the far-field radiation patterns. The radiation patterns can be studied by Fourier imaging. As shown by Shegai et al.,[72] the SERS emission is distributed in all the measured directions in a trimer system. Also, Zhu et al.[73] show in a dimer antenna on a glass and dielectric interface system that the simulated emission patterns radiate power into the substrate, with the emission angle distribution exceeding the critical angle for total internal reflection at the air-dielectric interface. Thus, the nanoislands on the tapered fiber surface facilitate Raman emission into the fiber with a wide angular distribution. The portion of light with angles within the fiber's collection capability, limited by the fiber's numerical aperture (NA), is collected and forms guided modes within the fiber, which then propagate back for detection. For a more comprehensive analysis of plasmonic fiber, Kim et al.[74] simulated dimer systems on top of the flat fiber. Factors including the particle geometry, excitation laser wavelength, refractive index, and NA of the fiber have been discussed, elaborating the importance of engineering the plasmonic "hot

https://doi.org/10.1021/acsphotonics.4c00912
ACS Photonics 2024, 11, 3774−3783

spot" close to optical fibers, deepening the understanding of particle-decorated fiber detection systems.

In summary, within the bottom-up methods to decorate nanoparticles on the tapered fiber tip, the tunable solid-state dewetting technology offers an effective and robust way to fabricate surfactant-free, well-defined, uniformly distributed, and densely packed monolayer NIs with controllable geometric parameters. Together with potential applications in remote detection schemes, the unique geometrical tunability helps in better understanding the correlation between particle size and density versus the electromagnetic performance of the probes, showing the electromagnetic part of the SERS performance of the probe can be optimized by maximizing the total VFE, other than the maximum field enhancement within the gaps. With the analyzable electromagnetic performance of the probe, the potential plasmonic-driven chemical reactions concerning monoamine neurotransmitters can be recognized. We believe our work introduces a versatile method for designing remote SERS sensing probes using nanoparticles, offering new experimental insights into surface interactions driven by plasmonic resonances.

METHODS

Tunable NIs-TF Set Fabrication. The TFs were fabricated from the standard multimode silica optical fibers (FG200LEA, 0.22 NA, Low−OH, Ø200 μm Core). To start with, the silica fibers were cut to a fixed length of 12 cm, then all the fibers were put in an acetone bath for 30 min to remove the acrylate jacket. Using the puller system (Sutter P-2000), the silica fibers were pulled rapidly, during the pulling process, the high temperature (above the silica transition temperature of 1207 °C) resulted in a clean and smooth TF surface before evaporation. After the silica TFs were prepared, all the TFs were sent to an e-beam evaporator for Au thin film deposition (Thermionics Laboratory, inc. e-GunTM). During the evaporation, all the TFs were mounted on a rotational motor to ensure conformal gold evaporation over the entire TFs' surfaces. The evaporation rate of 0.2 Å/s was used for all the depositions, with chamber pressure $<8 \times 10^{-7}$ mbar. For a batch of the tunable NIs-TFs set fabrication, around 40 blank silica fibers were placed in the chamber for the thin film deposition. Once the first layer of gold with a nominal thickness of Thk_1 = 1.7 nm was deposited, 10 thin film-deposited TFs were extracted from the chamber. Subsequently, a second layer of gold was deposited on top of the remaining TFs, contributing to a combined thickness of Thk_2 = 3.3 nm. After this deposition, another 10 TFs were withdrawn from the chamber. This process was iterated to generate two additional batches of TFs, each with deposition thicknesses of Thk_3 = 5.0 nm and Thk_4 = 6.7 nm, respectively. For the film thickness control, the TFs were linked to flat surface evaporation with the relation $T_{\mathrm{TFs}} = 1/\pi \times T_{\mathrm{Flat}}$, and thus, for Thk = 1.7, 3.3, 5, and 6.7 nm gold film deposition on TFs, the film sensor of the evaporator monitors 5, 10, 15, 20 nm of Au deposition. When the evaporation procedure finished, the fibers were detached from the mount and arranged in a ceramic bowl without any adhesive for thermal annealing in a muffle furnace (Nabertherm B180). The furnace was set to gradually ramp up from room temperature (RT) to 600 °C with a rate of 10 °C min^{-1}, and held at 600 °C for 1h, then allowed to cool ambiently to RT. Eventually, the nonstructured side of fabricated fibers was connected to metallic ferrules with a diameter of 1.25 mm, and went through a manual polishing process.

Morphological Analysis of Tunable NI Patterns. For the morphological analysis, SEM images were acquired with the FEI Helios Nanolab 600i Dual Beam system. The SEM image acquisitions were conducted after sputtering a thin layer of gold on all the NIs surfaces to provide sufficient conductivity. The sampling of the images was done through the entire extent of the fiber, and the number of samplings is no less than 10. Home-developed MATLAB programs were used for morphological analysis. The NIs number count and the coverage situations are obtained by a combined method of tracing object boundaries and circular Hough transform. Eventually, the coverage rates (C) and the average areas of physical occupation (S) were extracted, and thus, the average diameters can be determined by $D = 2\sqrt{S/\pi}$. The average height (H) of the NIs can be computed by $H = \mathrm{Thk}/C$, where Thk is the initial film deposition thickness. We have included a detailed description in section S1, and the analysis program is available on reasonable request.

Electromagnetic Simulations. The geometric parameters obtained from morphological analysis, including average diameters (D), height (H), and coverage rate (C), were used to build up a simplified numerical model with COMSOL Multiphysics, to emphasize the effect of the interparticle distances and reduce the computational cost. Thus, each pattern is represented with Au disks arranged in a periodic hexagonal array, with Au disks (all with diameter D) in the center of the hexagonal unit cell. To mimic the droplet-like shape of the fabricated sample, we have rounded the top edge of the disk with a radius of curvature $r = H \times 10\%$. In the 2D plane of the hexagonal unit cell, C is defined as the ratio between the gold disk area and the hexagonal unit cell area. In this picture, we can deduce the effective gap (G) as

$$G = D\left(\sqrt{\frac{\sqrt{3}\,\pi}{6C}} - 1\right)$$

By simulating three-dimensional time-harmonic Maxwell's equations, we obtained the results in Figure 3. The particle sits on an infinite dielectric substrate with a refractive index n = 1.4. Optical constants of gold were obtained from ref.[75] The mesh resolution is chosen so that transmittance results are converged to <0.1% at resonance.

The spectral response was obtained by scanning the source's wavelength from 400 to 900 nm, while field enhancement maps were generated at 785 nm, a widely employed wavelength for Raman inspection of biological samples.

To determine the number of unit cells (N) occupying the whole TF surface for 4 patterns, the tapered fibers were considered as a right circular cone with the diameter of its base d = 220 μm, its height h = 2.2 mm, thus we can calculate the surface area (s) as

$$s = \frac{\pi d}{2}\sqrt{h^2 + \left(\frac{d}{2}\right)^2} = 761215\ \mu\mathrm{m}^2$$

The NIs densities are 2895, 1872, 507, and 236 NIs/$\mu\mathrm{m}^2$ for four patterns obtained from SEM image analysis in Figure 2e, thus $N = [2.2037, 1.4250, 0.3859, 0.1796] \times 10^9$.

Through-Fiber SERS Characterizations. The optical setup for the home-built Raman microscope is shown in Figure S4. briefly, the linear polarized free space laser of 785

https://doi.org/10.1021/acsphotonics.4c00912
ACS Photonics 2024, 11, 3774−3783

nm continuous wavelength was coupled into a meter-long fiber patch cord to launch the laser into the excitation path of the Raman microscope, the resulting excitation laser delivered to the sample was scrambled into a speckle pattern.

The collimated laser beam filled the back aperture of the focus lens L1 (aspheric, Ø25.0 mm, f = 20 mm), resulting in a light spot of 200 μm in diameter, which matches the fiber core size. The fibers were configured with the distal end facing the focus lens, the laser was injected over the full angular acceptance of the fiber (NA 0.22) to recruit most of the propagating modes. The Raman signal, collected by the TF, was then separated from the pump laser using a dichroic mirror (DC: Semrock, LPD02-785RU-25) and a long-pass razor-edge filter (F1: Semrock, LP02-785RU-25). Then, the signal was routed to a spectrometer (Horiba iHR320). The Raman measurements were performed with a slit at 200 μm and a 600 lines/mm (blaze 750 nm) grating. Spectra were recorded on a SYNAPSE CCD cooled to −50 °C. All the raw spectra were treated with baseline correction (ALS). In the through-TFs SERS measurements. The laser power used for all measurements is 68 mW, the spectra acquisition time ranges between 30 to 180 s, and for analyzed data sets, all spectra intensity were normalized to 60 s exposure time. R6G (rhodamine 6G, $C_{28}H_{31}N_2O_3Cl$) and serotonin (5-hydroxytryptamine, $C_{10}H_{12}N_2O$) were all purchased from Merck KGaA.

■ ASSOCIATED CONTENT

Supporting Information

The Supporting Information is available free of charge at https://pubs.acs.org/doi/10.1021/acsphotonics.4c00912.

Tunable NI pattern morphological analysis (section S1), electromagnetic simulations (section S2), optical setup for the LOD measurements (section S3), and spectral data analysis for R6G and serotonin (section S4) (PDF)

■ AUTHOR INFORMATION

Corresponding Authors

Di Zheng − *Center for Biomolecular Nanotechnologies, Istituto Italiano di Tecnologia, 73010 Arnesano, Italy; State Key Laboratory of Radio Frequency Heterogeneous Integration, Shenzhen University, Shenzhen 518060, China;* orcid.org/0000-0002-9075-1857; Email: dr.zhengdi@outlook.com

Massimo De Vittorio − *Center for Biomolecular Nanotechnologies, Istituto Italiano di Tecnologia, 73010 Arnesano, Italy; Dipartimento di Ingegneria Dell'Innovazione, Università del Salento, 73100 Lecce, Italy; RAISE Ecosystem, 16122 Genova, Italy;* Email: massimo.devittorio@iit.it

Ferruccio Pisanello − *Center for Biomolecular Nanotechnologies, Istituto Italiano di Tecnologia, 73010 Arnesano, Italy; RAISE Ecosystem, 16122 Genova, Italy;* orcid.org/0000-0002-1489-7758; Email: Ferruccio.pisanello@iit.it

Authors

Muhammad Fayyaz Kashif − *Center for Biomolecular Nanotechnologies, Istituto Italiano di Tecnologia, 73010 Arnesano, Italy*

Linda Piscopo − *Center for Biomolecular Nanotechnologies, Istituto Italiano di Tecnologia, 73010 Arnesano, Italy; Dipartimento di Ingegneria Dell'Innovazione, Università del Salento, 73100 Lecce, Italy*

Liam Collard − *Center for Biomolecular Nanotechnologies, Istituto Italiano di Tecnologia, 73010 Arnesano, Italy; RAISE Ecosystem, 16122 Genova, Italy*

Cristian Ciracì − *Center for Biomolecular Nanotechnologies, Istituto Italiano di Tecnologia, 73010 Arnesano, Italy;* orcid.org/0000-0003-3349-8389

Complete contact information is available at: https://pubs.acs.org/10.1021/acsphotonics.4c00912

Author Contributions

⊥M.D.V. and F.P. contributed equally to this work.

Notes

The authors declare the following competing financial interest(s): M.D.V. and Fe.P. are founders and hold private equity in Optogenix, a company that develops, produces, and sells technologies to deliver light into the brain.

■ ACKNOWLEDGMENTS

M.D.V. and F.P. jointly supervised and are co-last authors in this work. D.Z., M.F.K., L.P., L.C., C.C., M.D.V., and F.P. acknowledge funding from the European Union's Horizon 2020 Research and Innovation Programme under Grant Agreement 828972. L.C., M.D.V., and F.P. acknowledge funding from the Project "RAISE (Robotics and AI for Socio-economic Empowerment)" (code ECS00000035) funded by European Union − NextGenerationEU PNRR MUR − M4C2 − Investimento 1.5 − Avviso "Ecosistemi dell'Innovazione" CUP J33C22001220001. F.P. acknowledges funding from the European Research Council under the European Union's Horizon 2020 Research and Innovation Programme under Grant Agreement 677683. M.D.V. and F.P. acknowledge that this project received funding from the European Union's Horizon 2020 Research and Innovation Programme under Grant Agreement 101016787. F.P. and M.D.V. were funded by the U.S. National Institutes of Health (Grant 1UF1NS108177-01).

■ REFERENCES

(1) Choi, N.; Schlücker, S. Convergence of Surface-Enhanced Raman Scattering with Molecular Diagnostics: A Perspective on Future Directions. *ACS Nano* **2024**, *18* (8), 5998−6007.

(2) Chen, C.; Wang, X.; Wang, R.; Waterhouse, G. I. N.; Xu, Z. SERS-Tag Technology in Food Safety and Detection: Sensing from the "Fingerprint" Region to the "Biological-Silent" Region. *J. Future Foods* **2024**, *4* (4), 309−323.

(3) Vázquez-Iglesias, L.; Stanfoca Casagrande, G. M.; García-Lojo, D.; Ferro Leal, L.; Ngo, T. A.; Pérez-Juste, J.; Reis, R. M.; Kant, K.; Pastoriza-Santos, I. SERS Sensing for Cancer Biomarker: Approaches and Directions. *Bioact. Mater.* **2024**, *34*, 248−268.

(4) Ong, T. T. X.; Blanch, E. W.; Jones, O. A. H. Surface Enhanced Raman Spectroscopy in Environmental Analysis, Monitoring and Assessment. *Sci. Total Environ.* **2020**, *720*, No. 137601.

(5) Bergholt, M. S.; Zheng, W.; Ho, K. Y.; Teh, M.; Yeoh, K. G.; So, J. B. Y.; Shabbir, A.; Huang, Z. Fiber-Optic Raman Spectroscopy Probes Gastric Carcinogenesis in Vivo at Endoscopy. *J. Biophotonics* **2013**, *6* (1), 49−59.

(6) McGregor, H. C.; Short, M. A.; Lam, S.; Shaipanich, T.; Beaudoin, E.-L.; Zeng, H. Development and in Vivo Test of a Miniature Raman Probe for Early Cancer Detection in the Peripheral Lung. *J. Biophotonics* **2018**, *11* (11), No. e201800055.

(7) Fortuni, B.; Ricci, M.; Vitale, R.; Inose, T.; Zhang, Q.; Hutchison, J. A.; Hirai, K.; Fujita, Y.; Toyouchi, S.; Krzyzowska, S.;

Van Zundert, I.; Rocha, S.; Uji-i, H. SERS Endoscopy for Monitoring Intracellular Drug Dynamics. *ACS Sens.* **2023**, *8* (6), 2340−2347.
(8) Zhang, Q.; Inose, T.; Ricci, M.; Li, J.; Tian, Y.; Wen, H.; Toyouchi, S.; Fron, E.; Ngoc Dao, A. T.; Kasai, H.; Rocha, S.; Hirai, K.; Fortuni, B.; Uji-i, H. Gold-Photodeposited Silver Nanowire Endoscopy for Cytosolic and Nuclear pH Sensing. *ACS Appl. Nano Mater.* **2021**, *4* (9), 9886−9894.
(9) Zhang, H.; Zhou, X.; Li, X.; Gong, P.; Zhang, Y.; Zhao, Y. Recent Advancements of LSPR Fiber-Optic Biosensing: Combination Methods, Structure, and Prospects. *Biosensors* **2023**, *13* (3), 405.
(10) Liu, Y.; Lin, C.; Chen, H.; Shen, C.; Zheng, Z.; Li, M.; Xu, B.; Zhao, C.; Kang, J.; Wang, Y. A Rapid Surface-Enhanced Raman Scattering Method for the Determination of Trace Hg^{2+} with Tapered Optical Fiber Probe. *Microchem. J.* **2024**, *196*, No. 109724.
(11) Lyu, D.; Huang, Q.; Wu, X.; Nie, Y.; Yang, M. Optical Fiber Sensors for Water and Air Quality Monitoring: A Review. *Opt. Eng.* **2024**, *63* (3), No. 031004.
(12) Zheng, D.; Pisano, F.; Collard, L.; Balena, A.; Pisanello, M.; Spagnolo, B.; Mach-Batlle, R.; Tantussi, F.; Carbone, L.; De Angelis, F.; Valiente, M.; de la Prida, L. M.; Ciracì, C.; De Vittorio, M.; Pisanello, F. Toward Plasmonic Neural Probes: SERS Detection of Neurotransmitters through Gold-Nanoislands-Decorated Tapered Optical Fibers with Sub-10 nm Gaps. *Adv. Mater.* **2023**, *35* (11), No. 2200902.
(13) Collard, L.; Pisano, F.; Zheng, D.; Balena, A.; Kashif, M. F.; Pisanello, M.; D'Orazio, A.; de la Prida, L. M.; Ciracì, C.; Grande, M.; De Vittorio, M.; Pisanello, F. Holographic Manipulation of Nanostructured Fiber Optics Enables Spatially-Resolved, Reconfigurable Optical Control of Plasmonic Local Field Enhancement and SERS. *Small* **2022**, *18* (23), No. 2200975.
(14) Lee, W.; Kang, B.-H.; Yang, H.; Park, M.; Kwak, J. H.; Chung, T.; Jeong, Y.; Kim, B. K.; Jeong, K.-H. Spread Spectrum SERS Allows Label-Free Detection of Attomolar Neurotransmitters. *Nat. Commun.* **2021**, *12* (1), 159.
(15) Malhi, G. S.; Mann, J. J. Depression. *Lancet* **2018**, *392* (10161), 2299−2312.
(16) McCutcheon, R. A.; Krystal, J. H.; Howes, O. D. Dopamine and Glutamate in Schizophrenia: Biology, Symptoms and Treatment. *World Psychiatry* **2020**, *19* (1), 15−33.
(17) Segura-Aguilar, J.; Paris, I.; Muñoz, P.; Ferrari, E.; Zecca, L.; Zucca, F. A. Protective and Toxic Roles of Dopamine in Parkinson's Disease. *J. Neurochem.* **2014**, *129* (6), 898−915.
(18) Xu, Y.; Yan, J.; Zhou, P.; Li, J.; Gao, H.; Xia, Y.; Wang, Q. Neurotransmitter Receptors and Cognitive Dysfunction in Alzheimer's Disease and Parkinson's Disease. *Prog. Neurobiol.* **2012**, *97* (1), 1−13.
(19) Du, W.; Wei, S.; Li, N.; Hao, Z.; Li, Y.; Wang, M. Highly Sensitive Fiber Optic Enhanced Raman Scattering Sensor. *Opt. Laser Technol.* **2024**, *168*, No. 109879.
(20) Huang, R.; Lian, S.; Li, J.; Feng, Y.; Bai, S.; Wu, T.; Ruan, M.; Wu, P.; Li, X.; Cai, S.; Jiang, P. High-Sensitivity and Throughput Optical Fiber SERS Probes Based on Laser-Induced Fractional Reaction Method. *Results Phys.* **2023**, *48*, No. 106410.
(21) Yang, X.; Ileri, N.; Larson, C. C.; Carlson, T. C.; Britten, J. A.; Chang, A. S. P.; Gu, C.; Bond, T. C. Nanopillar Array on a Fiber Facet for Highly Sensitive Surface-Enhanced Raman Scattering. *Opt. Express* **2012**, *20* (22), 24819−24826.
(22) Huang, J.; Zhou, F.; Cai, C.; Chu, R.; Zhang, Z.; Liu, Y. Remote SERS Detection at a 10-m Scale Using Silica Fiber SERS Probes Coupled with a Convolutional Neural Network. *Opt. Lett.* **2023**, *48* (4), 896.
(23) Yu, Z.; Wang, Z.; Zhang, J. Preparation Optimization for a Silver Cavity Coupled Tapered Fiber SERS Probe with High Sensitivity. *Opt. Mater. Express* **2022**, *12* (7), 2835−2843.
(24) Tian, Q.; Cao, S.; He, G.; Long, Y.; Zhou, X.; Zhang, J.; Xie, J.; Zhao, X. Plasmonic Au-Ag Alloy Nanostars Based High Sensitivity Surface Enhanced Raman Spectroscopy Fiber Probes. *J. Alloys Compd.* **2022**, *900*, No. 163345.
(25) Kang, T.; Cho, Y.; Yuk, K. M.; Yu, C. Y.; Choi, S. H.; Byun, K. M. Fabrication and Characterization of Novel Silk Fiber-Optic SERS Sensor with Uniform Assembly of Gold Nanoparticles. *Sensors* **2022**, *22* (22), 9012.
(26) He, G.; Han, X.; Cao, S.; Cui, K.; Tian, Q.; Zhang, J. Long Spiky Au-Ag Nanostar Based Fiber Probe for Surface Enhanced Raman Spectroscopy. *Materials* **2022**, *15* (4), 1498.
(27) Yu, M.; Tian, Q.; He, G.; Cui, K.; Zhang, J. Surface-Enhanced Raman Scattering Fiber Probe Based on Silver Nanocubes. *Adv. Fiber Mater.* **2021**, *3* (6), 349−358.
(28) Zhou, F.; Liu, Y.; Wang, H.; Wei, Y.; Zhang, G.; Ye, H.; Chen, M.; Ling, D. Au-Nanorod-Clusters Patterned Optical Fiber SERS Probes Fabricated by Laser-Induced Evaporation Self-Assembly Method. *Opt. Express* **2020**, *28* (5), 6648−6662.
(29) Kim, J. A.; Wales, D. J.; Thompson, A. J.; Yang, G.-Z. Fiber-Optic SERS Probes Fabricated Using Two-Photon Polymerization For Rapid Detection of Bacteria. *Adv. Opt. Mater.* **2020**, *8* (9), No. 1901934.
(30) Kwak, J.; Lee, W.; Kim, J.-B.; Bae, S.-I.; Jeong, K.-H. Fiber-Optic Plasmonic Probe with Nanogap-Rich Au Nanoislands for on-Site Surface-Enhanced Raman Spectroscopy Using Repeated Solid-State Dewetting. *J. Biomed. Opt.* **2019**, *24* (3), No. 037001.
(31) Xia, M.; Zhang, P.; Leung, C.; Xie, Y.-H. SERS Optical Fiber Probe with Plasmonic End-Facet. *J. Raman Spectrosc.* **2017**, *48* (2), 211−216.
(32) Pisanello, M.; Pisano, F.; Sileo, L.; Maglie, E.; Bellistri, E.; Spagnolo, B.; Mandelbaum, G.; Sabatini, B. L.; De Vittorio, M.; Pisanello, F. Tailoring Light Delivery for Optogenetics by Modal Demultiplexing in Tapered Optical Fibers. *Sci. Rep.* **2018**, *8* (1), 4467.
(33) Deng, Q.; Kang, M.; Zheng, D.; Zhang, S.; Xu, H. Mimicking Plasmonic Nanolaser Emission by Selective Extraction of Electromagnetic Near-Field from Photonic Microcavity. *Nanoscale* **2018**, *10* (16), 7431−7439.
(34) Densmore, A.; Xu, D.-X.; Janz, S.; Waldron, P.; Lapointe, J.; Mischki, T.; Lopinski, G.; Delâge, A.; Schmid, J. H.; Cheben, P. Sensitive Label-Free Biomolecular Detection Using Thin Silicon Waveguides. *Adv. Opt. Technol.* **2008**, *2008* (1), No. 725967.
(35) Pisano, F.; Pisanello, M.; Lee, S. J.; Lee, J.; Maglie, E.; Balena, A.; Sileo, L.; Spagnolo, B.; Bianco, M.; Hyun, M.; De Vittorio, M.; Sabatini, B. L.; Pisanello, F. Depth-Resolved Fiber Photometry with a Single Tapered Optical Fiber Implant. *Nat. Methods* **2019**, *16* (11), 1185−1192.
(36) Qin, Y.; Huang, R.; Lu, F.; Tang, H.; Yao, B.; Mao, Q. Effects of the Cone Angle on the SERS Detection Sensitivity of Tapered Fiber Probes. *Opt. Express* **2022**, *30* (21), 37507−37518.
(37) Li, T.; Yu, Z.; Wang, Z.; Zhu, Y.; Zhang, J. Optimized Tapered Fiber Decorated by Ag Nanoparticles for Raman Measurement with High Sensitivity. *Sensors* **2021**, *21* (7), 2300.
(38) Zhu, H.; Masson, J.-F.; Bazuin, C. G. Templating Gold Nanoparticles on Nanofibers Coated with a Block Copolymer Brush for Nanosensor Applications. *ACS Appl. Nano Mater.* **2020**, *3* (1), 516−529.
(39) Hutter, T.; Elliott, S. R.; Mahajan, S. Optical Fibre-Tip Probes for SERS: Numerical Study for Design Considerations. *Opt. Express* **2018**, *26* (12), 15539.
(40) Xu, W.; Chen, Z.; Chen, N.; Zhang, H.; Liu, S.; Hu, X.; Wen, J.; Wang, T. SERS Taper-Fiber Nanoprobe Modified by Gold Nanoparticles Wrapped with Ultrathin Alumina Film by Atomic Layer Deposition. *Sensors* **2017**, *17* (3), 467.
(41) Lussier, F.; Brulé, T.; Bourque, M.-J.; Ducrot, C.; Trudeau, L.-É.; Masson, J.-F. Dynamic SERS Nanosensor for Neurotransmitter Sensing near Neurons. *Faraday Discuss.* **2017**, *205*, 387−407.
(42) Huang, Z.; Lei, X.; Liu, Y.; Wang, Z.; Wang, X.; Wang, Z.; Mao, Q.; Meng, G. Tapered Optical Fiber Probe Assembled with Plasmonic Nanostructures for Surface-Enhanced Raman Scattering Application. *ACS Appl. Mater. Interfaces* **2015**, *7* (31), 17247−17254.
(43) Chen, Z.; Dai, Z.; Chen, N.; Liu, S.; Pang, F.; Lu, B.; Wang, T. Gold Nanoparticles-Modified Tapered Fiber Nanoprobe for Remote

SERS Detection. *IEEE Photonics Technol. Lett.* **2014**, *26* (8), 777−780.
(44) Cao, J.; Zhao, D.; Qin, Y. Novel Strategy for Fabrication of Sensing Layer on Thiol-Functionalized Fiber-Optic Tapers and Their Application as SERS Probes. *Talanta* **2019**, *194*, 895−902.
(45) Cao, J.; Zhao, D.; Mao, Q. A Highly Reproducible and Sensitive Fiber SERS Probe Fabricated by Direct Synthesis of Closely Packed AgNPs on the Silanized Fiber Taper. *Analyst* **2017**, *142* (4), 596−602.
(46) Zhang, J.; Chen, S.; Gong, T.; Zhang, X.; Zhu, Y. Tapered Fiber Probe Modified by Ag Nanoparticles for SERS Detection. *Plasmonics* **2016**, *11* (3), 743−751.
(47) Cao, J.; Zhao, D.; Mao, Q. Laser-Induced Synthesis of Ag Nanoparticles on the Silanized Surface of a Fiber Taper and Applications as a SERS Probe. *RSC Adv.* **2015**, *5* (120), 99491−99497.
(48) Volkan, M.; Stokes, D. L.; Vo-Dinh, T. Surface-Enhanced Raman of Dopamine and Neurotransmitters Using Sol-Gel Substrates and Polymer-Coated Fiber-Optic Probes. *Appl. Spectrosc.* **2000**, *54* (12), 1842−1848.
(49) Liu, Y.; Liu, R.; Ai, C.; Wang, B.; Chu, R.; Wang, H.; Shui, L.; Zhou, F. Stick-Slip-Motion-Assisted Interfacial Self-Assembly of Noble Metal Nanoparticles on Tapered Optical Fiber Surface and Its Application in SERS Detection. *Appl. Surf. Sci.* **2022**, *602*, No. 154298.
(50) Tao, P.; Ge, K.; Dai, X.; Xue, D.; Luo, Y.; Dai, S.; Xu, T.; Jiang, T.; Zhang, P. Fiber Optic SERS Sensor with Silver Nanocubes Attached Based on Evanescent Wave for Detecting Pesticide Residues. *ACS Appl. Mater. Interfaces* **2023**, *15* (25), 30998−31008.
(51) Kaur, N.; Das, G. Three-Dimensional Plasmonic Substrate as Surface-Enhanced Raman Spectroscopy (SERS) Tool for the Detection of Trace Chemicals. *J. Raman Spectrosc.* **2024**, *55* (4), 473−480.
(52) Mohammad-Zadeh, L. F.; Moses, L.; Gwaltney-Brant, S. M. Serotonin: A Review. *J. Vet. Pharmacol. Ther.* **2008**, *31* (3), 187−199.
(53) Zhao, S.; Piatkevich, K. D. Techniques for in Vivo Serotonin Detection in the Brain: State of the Art. *J. Neurochem.* **2023**, *166* (3), 453−480.
(54) He, X. N.; Gao, Y.; Mahjouri-Samani, M.; Black, P. N.; Allen, J.; Mitchell, M.; Xiong, W.; Zhou, Y. S.; Jiang, L.; Lu, Y. F. Surface-Enhanced Raman Spectroscopy Using Gold-Coated Horizontally Aligned Carbon Nanotubes. *Nanotechnology* **2012**, *23* (20), No. 205702.
(55) Lu, R.; Konzelmann, A.; Xu, F.; Gong, Y.; Liu, J.; Liu, Q.; Xin, M.; Hui, R.; Wu, J. Z. High Sensitivity Surface Enhanced Raman Spectroscopy of R6G on *in Situ* Fabricated Au Nanoparticle/Graphene Plasmonic Substrates. *Carbon* **2015**, *86*, 78−85.
(56) Bain, A. J.; Chandna, P.; Butcher, G.; Bryant, J. Picosecond Polarized Fluorescence Studies of Anisotropic Fluid Media. II. Experimental Studies of Molecular Order and Motion in Jet Aligned Rhodamine 6G and Resorufin Solutions. *J. Chem. Phys.* **2000**, *112* (23), 10435−10449.
(57) López Arbeloa, F.; Martínez Martínez, V.; Arbeloa, T.; López Arbeloa, I. Photoresponse and Anisotropy of Rhodamine Dye Intercalated in Ordered Clay Layered Films. *J. Photochem. Photobiol. C.* **2007**, *8* (2), 85−108.
(58) Rocchigiani, L.; Bochmann, M. Recent Advances in Gold(III) Chemistry: Structure, Bonding, Reactivity, and Role in Homogeneous Catalysis. *Chem. Rev.* **2021**, *121* (14), 8364−8451.
(59) Feng, J.; Pandey, R. B.; Berry, R. J.; Farmer, B. L.; Naik, R. R.; Heinz, H. Adsorption Mechanism of Single Amino Acid and Surfactant Molecules to Au {111} Surfaces in Aqueous Solution: Design Rules for Metal-Binding Molecules. *Soft Matter* **2011**, *7* (5), 2113−2120.
(60) Hoefling, M.; Iori, F.; Corni, S.; Gottschalk, K.-E. The Conformations of Amino Acids on a Gold(111) Surface. *ChemPhysChem* **2010**, *11* (8), 1763−1767.
(61) Zhong, Z.; Patskovskyy, S.; Bouvrette, P.; Luong, J. H. T.; Gedanken, A. The Surface Chemistry of Au Colloids and Their Interactions with Functional Amino Acids. *J. Phys. Chem. B* **2004**, *108* (13), 4046−4052.
(62) Lyu, Y.; Becerril, L. M.; Vanzan, M.; Corni, S.; Cattelan, M.; Granozzi, G.; Frasconi, M.; Rajak, P.; Banerjee, P.; Ciancio, R.; Mancin, F.; Scrimin, P. The Interaction of Amines with Gold Nanoparticles. *Adv. Mater.* **2024**, *36* (10), No. 2211624.
(63) Lowe, A. B. Thiol-Ene "Click" Reactions and Recent Applications in Polymer and Materials Synthesis. *Polym. Chem.* **2010**, *1* (1), 17−36.
(64) Do, P. Q. T.; Huong, V. T.; Phuong, N. T. T.; Nguyen, T.-H.; Ta, H. K. T.; Ju, H.; Phan, T. B.; Phung, V.-D.; Trinh, K. T. L.; Tran, N. H. T. The Highly Sensitive Determination of Serotonin by Using Gold Nanoparticles (Au NPs) with a Localized Surface Plasmon Resonance (LSPR) Absorption Wavelength in the Visible Region. *RSC Adv.* **2020**, *10* (51), 30858−30869.
(65) Wang, P.; Xia, M.; Liang, O.; Sun, K.; Cipriano, A. F.; Schroeder, T.; Liu, H.; Xie, Y.-H. Label-Free SERS Selective Detection of Dopamine and Serotonin Using Graphene-Au Nanopyramid Heterostructure. *Anal. Chem.* **2015**, *87* (20), 10255−10261.
(66) Moody, A. S.; Sharma, B. Multi-Metal, Multi-Wavelength Surface-Enhanced Raman Spectroscopy Detection of Neurotransmitters. *ACS Chem. Neurosci.* **2018**, *9* (6), 1380−1387.
(67) Qiu, C.; Bennet, K. E.; Tomshine, J. R.; Hara, S.; Ciubuc, J. D.; Schmidt, U.; Durrer, W. G.; McIntosh, M. B.; Eastman, M.; Manciu, F. S. Ultrasensitive Detection of Neurotransmitters by Surface Enhanced Raman Spectroscopy for Biosensing Applications. *Biointerface Res. Appl. Chem.* **2017**, *7* (1), 1921−1926.
(68) Choi, H.-K.; Park, W.-H.; Park, C.-G.; Shin, H.-H.; Lee, K. S.; Kim, Z. H. Metal-Catalyzed Chemical Reaction of Single Molecules Directly Probed by Vibrational Spectroscopy. *J. Am. Chem. Soc.* **2016**, *138* (13), 4673−4684.
(69) Shin, H.-H.; Jeong, J.; Nam, Y.; Lee, K. S.; Yeon, G. J.; Lee, H.; Lee, S. Y.; Park, S.; Park, H.; Lee, J. Y.; Kim, Z. H. Vibrationally Hot Reactants in a Plasmon-Assisted Chemical Reaction. *J. Am. Chem. Soc.* **2023**, *145* (22), 12264−12274.
(70) Kazuma, E. Key Factors for Controlling Plasmon-Induced Chemical Reactions on Metal Surfaces. *J. Phys. Chem. Lett.* **2024**, *15* (1), 59−67.
(71) Masson, J.-F.; Wallace, G. Q.; Asselin, J.; Ten, A.; Hojjat Jodaylami, M.; Faulds, K.; Graham, D.; Biggins, J. S.; Ringe, E. Optoplasmonic Effects in Highly Curved Surfaces for Catalysis, Photothermal Heating, and SERS. *ACS Appl. Mater. Interfaces* **2023**, *15* (39), 46181−46194.
(72) Shegai, T.; Brian, B.; Miljković, V. D.; Käll, M. Angular Distribution of Surface-Enhanced Raman Scattering from Individual Au Nanoparticle Aggregates. *ACS Nano* **2011**, *5* (3), 2036−2041.
(73) Zhu, W.; Wang, D.; Crozier, K. B. Direct Observation of Beamed Raman Scattering. *Nano Lett.* **2012**, *12* (12), 6235−6243.
(74) Kim, S.; Gomes, O. P.; De Koninck, Y.; Messaddeq, Y. A Comprehensive Numerical Study on Fiber Optic SERS Probe Design. *J. Phys. Chem. C* **2024**, *128* (15), 6357−6369.
(75) Olmon, R. L.; Slovick, B.; Johnson, T. W.; Shelton, D.; Oh, S.-H.; Boreman, G. D.; Raschke, M. B. Optical Dielectric Function of Gold. *Phys. Rev. B* **2012**, *86* (23), No. 235147.

https://doi.org/10.1021/acsphotonics.4c00912
ACS Photonics 2024, 11, 3774−3783